


Nature of Point Defects in Single-Layer MoS₂ Supported on Au(111)

Francesco Tumino, Carlo Spartaco Casari, Andrea Li Bassi, and Sergio Tosoni*


 Cite This: *J. Phys. Chem. C* 2020, 124, 12424–12431

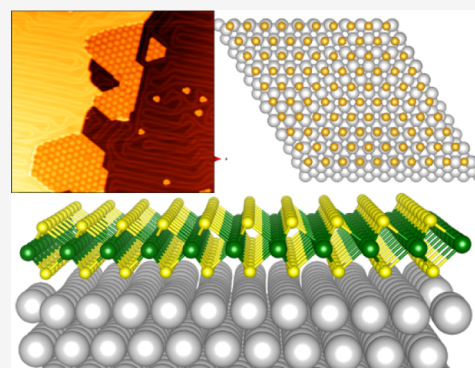

 Read Online

ACCESS |


 Metrics & More


 Article Recommendations

ABSTRACT: The interaction between molybdenum disulfide monolayers and gold is studied by combining scanning tunneling microscopy (STM) measurements on extended MoS₂ films grown by pulsed laser deposition and density functional theory (DFT) calculations. The lattice mismatch between MoS₂ and Au leads to the growth of extended monolayer films displaying a noncommensurate lattice with the metal substrate. STM images are also characterized by a high concentration of features related to two kinds of point defects. DFT calculations highlight the role of the local MoS₂/Au registry in driving the film–substrate interaction, showing that in the regions of the moiré superlattice where a top coincidence is found, Au atoms are lifted up to some extent as a result of the interaction with the MoS₂ film, reducing remarkably the interfacial distance. The combination of *ab initio* thermodynamics and Tersoff–Hamann simulated images permits us to assign the most commonly observed defect features to single-sulfur vacancies located either on the outer surface or at the interface with gold. This fact has important implications on the conductivity and catalytic properties of this material.



1. INTRODUCTION

Transition-metal dichalcogenides are solid materials characterized by weakly bound layered structures. Each layer is typically composed by a sheet of a transition metal enclosed between sheets of two chalcogenides.¹ They are easily prone to exfoliation, forming two-dimensional monolayers. In particular, molybdenum disulfide attracted a considerable interest for its optical,² electronic,^{3,4} and catalytic properties.^{5–7} Both electronic and chemical properties have been proven to remarkably depend on structural aspects such as the strain⁸ or the presence of point defects.^{9–11} Also, the mobility of electrons and holes is increased in defective MoS₂ compared to the pristine one,¹⁰ with relevant implications in microelectronics.

A well-consolidated technique to study in detail about the morphology and properties of thin films and 2D materials consists in promoting their growth under controlled conditions over metal supports, which enables us to employ electron microscopies and spectroscopies.^{12,13} MoS₂ monolayers (MLs) have been studied in interaction to several metal supports, including gold.^{14–17} The most stable gold surface, Au(111), is well known for its chemical inertness, strong electronegativity, and large-scale reconstruction, characterized by the presence of two stacking domains, the hexagonal close-packed (hcp) and the face-centered cubic (fcc), which rotate periodically by 120° forming its well-known “herringbone” pattern.^{18,19} This structure influences the growth pattern of MoS₂ ML, which tends to form triangular or hexagonal islands confined to the terrace regions of reconstructed Au(111), thus lifting the herringbone structure. Extended ML islands crossing the

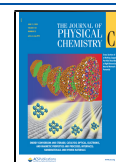
herringbone’s ridges are commonly not observed, as also previously reported.^{20–22} The lattice mismatch between the substrate and the supported dichalcogenide film leads to a moiré pattern because of the different vertical Au–S–Mo–S stacking. This pattern is typically detected by AFM or STM measurements as succession of hexagonal brighter and darker regions with a periodicity of $33 \pm 1 \text{ \AA}$.²² In spite of the substantial chemical inertness of the support, hybridization and screening effects because of the interaction with the Au support, depending on the local film/support match, affect remarkably the electronic structure of MoS₂.^{17,21} It is still matter of debate, however, if these electronic effects correspond to relevant changes in the topographic MoS₂ profile.²²

An intriguing feature of MoS₂ film growth on Au is the relatively abundant presence of point defects, with potential interesting consequences on the chemical activity of these structures. Recent STM measurements of monolayer MoS₂/Au(111) made by pulsed laser deposition (PLD) revealed two different features, appearing as circular or triangular darker spots on the pattern of the surface, tentatively assigned to sulfur vacancies and MoS₃ vacancies, respectively.²²

Received: February 20, 2020

Revised: April 22, 2020

Published: May 19, 2020



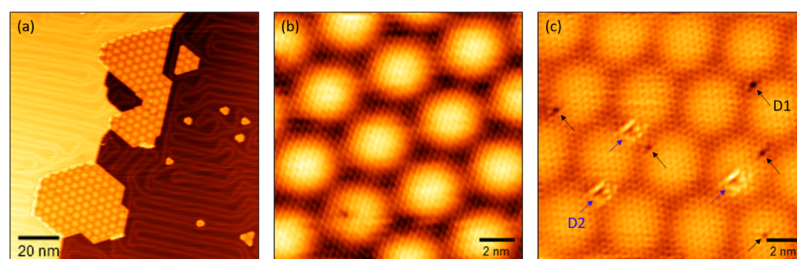


Figure 1. Constant-current STM images of ML MoS₂/Au(111). (a) Large-scale image showing two relatively large MoS₂ crystallites attached to the Au step edge and smaller islands growing on the Au terrace. Notice that the herringbone ridges are distorted by MoS₂ islands, which tend to lift the Au(111) reconstruction. (b,c) High-resolution images showing (b) the hexagonal moiré pattern of ~ 33 Å periodicity (0.1 V, 1 nA) and (c) presence of point defects of different morphology labeled as D1 (black arrows) and D2 (blue arrows) (0.3 V, 1 nA; color contrast has been modified to enhance surface defects).

In the present paper, we performed density functional theory (DFT) calculations on a realistic model structure of the MoS₂/Au(111) superlattice to provide insights into the atomic-scale properties experimentally observed by STM. This work aims at clarifying the local morphology of the differently stacked regions and identifying the chemical nature of the most abundant point defects.

It must be acknowledged that point defects in MoS₂ have been previously studied both experimentally and theoretically.^{9–11,23–26} However, such a study for MoS₂/Au is hereby presented for the first time. This paper, moreover, goes beyond previous computational reports on this system^{11,17} because a large supercell actually accounting for the 33 ± 1 Å periodicity as revealed by experimental measurement is adopted. This ensures small residual strain at the oxide/metal interface, as discussed in the next section. This is an important aspect for a realistic modelling of MoS₂/Au because strain influences the physical properties of supported films, as shown for instance by means of Raman spectroscopy.²⁷ The possibility to simulate point defects in their actual environment at the interface with the support and in a realistically low concentration is also ensured. Moreover, an approach combining *ab initio* thermodynamics and simulation of STM images is used to reveal the nature of the most abundant point defects in this specific system, an aspect which is still a matter of debate.

2. EXPERIMENTAL AND COMPUTATIONAL METHODOLOGY

2.1. Experiments. Sample preparation and *in situ* STM/STS measurements were performed in an ultrahigh vacuum (UHV) system (base pressure 10^{-11} mbar). Au(111) on mica was cleaned by cycles of Ar⁺ sputtering (1 keV) and annealing (700 K). MoS₂ was grown on freshly prepared Au(111) by PLD in a dedicated vacuum chamber (base pressure 10^{-9} mbar), coupled to the STM system. A KrF laser (248 nm wavelength, 20 ns pulse duration) was used to ablate a stoichiometric MoS₂ target (Testbourne). The laser fluence was approximately 2 J/cm². The number of laser pulses (typically, between 5 and 20) was finely tuned to get the desired MoS₂ coverage in the monolayer range, following previous reports.²² During deposition, the Au substrate is at room temperature and placed 5 cm away from the target. After deposition, the sample is annealed at 730 K for 30 min in UHV. Constant-current STM images were acquired at room temperature using a VT-SPM Omicron microscope, equipped with homemade electrochemically etched W tips. Room-temperature STS measurements were performed in open-loop conditions using a lock-in amplifier operating at 4 kHz and 28 mV_{rms}.

2.2. DFT Calculations. All calculations are carried out in the general frame of the DFT on periodic models with the code VASP.^{28,29} The core electrons are treated with the projector augmented wave method,^{30,31} while Au(5d,6s), Mo(4p,4d,5s), and S(3s,3p) electrons are treated explicitly. The exchange–correlation functional proposed by Perdew, Burke, and Ernzerhof (PBE)³² is adopted. The long-range dispersion is added to the potential according to the DFT + D3 scheme.³³ Spin-polarization effects are included in all calculations on defective structures. The lattice relaxation of bulk Au and MoS₂ is carried out with a mesh of $6 \times 6 \times 6$ special *k*-points (MoS₂) and $12 \times 12 \times 12$ *k*-points (Au) and a kinetic cutoff of 600 eV. Subsequent relaxations of the electronic structure and ionic positions of MoS₂/Au interfaces are done at Γ point with a cutoff of 400 eV. The choice to reduce the sampling of the reciprocal space to the Γ point is justified by the very large dimension of the supercell (vide infra). A smearing of 0.1 eV is used to ensure convergence of the self-consistent field process. Dipole and quadrupole corrections to the total energy are applied along the nonperiodic direction for all calculations on slab models.³⁴ In order to avoid spurious interactions between replica of the slab models, a vacuum region of at least 15 Å is included along the nonperiodic direction in the supercell.

The relaxed lattice constant of Au (4.10 Å) is in good agreement with the experimental X-ray diffraction measurements (4.08 Å).³⁵ Also in the case of MoS₂ bulk, the PBE + D3 method yields lattice parameters ($a = b = 3.15$ Å, $c = 12.07$ Å) quite close to the experiment ($a = b = 3.16$ Å, $c = 12.29$ Å).³⁶ One can notice that the relaxation of the *c* lattice parameter, describing the interlayer distance dominated by dispersive interactions is slightly less accurate. As also previously documented in the literature, GGA functionals tend to underestimate the band gap of MoS₂. We yield a band gap of 0.84 eV (indirect) and 1.78 eV (direct) for bulk and ML MoS₂, respectively. This is in good agreement with previous GGA calculations (0.88 and 1.67 eV),⁸ while calculations based on the GW-quasiparticle approximation yield are 1.29 eV (bulk)³⁷ and 2.75–2.82 eV (ML),^{37–39} respectively. Experimentally, optical band gaps as large as 1.3 eV (bulk)⁴⁰ and 1.9 eV (ML)³ are reported.

The MoS₂ ML on Au(111) is simulated superimposing a 10×10 MoS₂ supercell on a 11×11 Au(111). The metal substrate is modelled as a four-layer slab, where the atoms of the bottom layer are kept fixed to their bulk position during the relaxation. The positions (both lateral and vertical) of the atoms belonging to the two Au upper layers and the MoS₂ film are fully relaxed. The lattice of the 10×10 MoS₂ is stretched by 1.18% to coincide with that of the 11×11 Au. There is thus a small residual lattice

strain released on the dichalcogenide film. The resulting superlattice periodicity is 31.9 Å. Experimentally, a periodicity of 33 ± 1 Å is observed. In some reports, a small reciprocal rotation between the substrate and the film is described, varying from 0.45^{41} to $2 \pm 1^\circ$.²² A film–substrate match free of any rotation was reported elsewhere.^{20,21} In the model adopted here for the simulations, no reciprocal rotation between MoS₂ and Au is considered.

3. RESULTS AND DISCUSSION

3.1. Interaction of ML MoS₂ Islands with the Substrate.

Constant-current STM images of MoS₂ ML crystals grown on Au(111) by PLD are shown in Figure 1. A representative large-scale STM image, reported in Figure 1a, shows relatively large MoS₂ crystallites attached to Au step edges, together with smaller islands growing on the Au terrace. The herringbone reconstruction is perturbed by MoS₂ growth: Figure 1a shows that MoS₂ islands tend to repel the herringbone ridges, thus lifting the Au(111) reconstruction, as also observed in previous reports.^{22,41} The atomic resolution image reported in Figure 1b shows both the hexagonal moiré pattern and the MoS₂ lattice. The different contrast regions within the moiré supercell suggest that the electronic structure is locally perturbed by the interaction between the film and the metal substrate. STM images taken over defective MoS₂ regions (Figure 1c) show the presence of two main types of point defects, looking either like dark and almost spherical spots (D1) or triangles with bright sides and a dark core (D2).²² From the analysis of larger scale images, we can estimate a surface defect density of $\sim 10^{12}/\text{cm}^2$, about half of which is D1-like and the other half is D2-like. This paper aims at elucidating these main features by combining STM measurements with DFT simulations.

We start the discussion by examining the simulation of the defect-free MoS₂ ML on Au(111). Top and side views of the relaxed structure of MoS₂/Au are reported in Figure 2a,b,

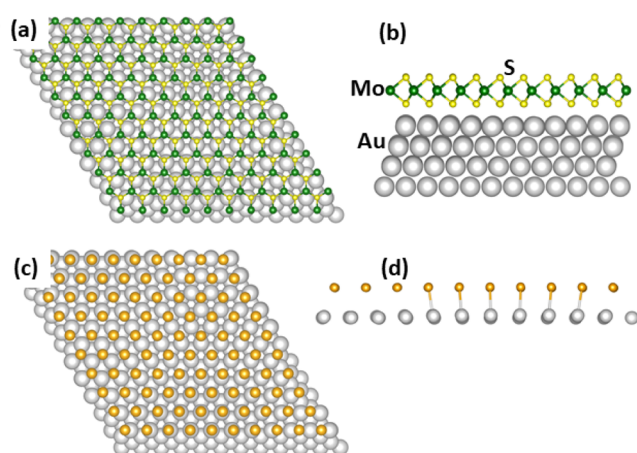


Figure 2. (a) Top view and (b) side view of MoS₂ ML supported on Au(111), ball and stick representation of the relaxed structure. (c) Top view and (d) side view of the Au–S coincidence at the interface (a cutoff distance of 2.6 Å has been adopted to draw the Au–S bonds).

respectively. Our model fully accounts for the experimentally observed moiré pattern, characterized by the alternations of domains where the bottom S atoms of the film are coordinated on top, bridge, (hcp and fcc) hollow sites, or in intermediate positions, as shown in Figure 2c. Interestingly, the film–substrate interfacial distance (calculated as the difference in

height between the S atoms from the bottom layer and the Au atoms from the topmost support's layer) remarkably depends on the local registry and is significantly shorter in the case of S–Au top coincidence (2.53 Å) with respect to hcp (2.73 Å) and fcc (2.69 Å) hollows. The average interfacial distance, mediated over the whole supercell, is 2.63 Å. These values, however, exceed from the range of covalent S–Au bonds, which span from 2.16 Å in the AuS molecule⁴² to 2.2–2.3 Å for thiols covalently bound to Au adatoms or Au surfaces.⁴³ This confirms that the MoS₂/Au interaction has a noncovalent character. The nature of this modulation can be further investigated by looking at the mean and maximum rumpling of the atoms belonging to the bottom S layer and the top Au layer. The rumpling is defined as the deviation of the vertical position of an atom from the average position of all atoms belonging to a given layer. Both the free-standing MoS₂ film and the clean Au(111) model surface display zero rumpling. For MoS₂/Au, the S atoms from the bottom layer have a very small mean rumpling of 0.02 Å and a maximum rumpling of 0.05 Å. For the topmost Au layer, we observe a mean and a maximum rumpling as large as 0.07 and 0.15 Å, respectively. The modulation of the Au–S interfacial distance as a function of the registry can also be seen in Figure 2d. The shorter interfacial distance observed in the case of top S–Au coincidence is thus mostly because of the uplifting of the Au atoms, as also resulting from the perturbation of the underlying herringbone reconstruction of Au(111) detected by STM^{16,22} and electron diffraction measurements.²⁰

In a previous report, Bruix *et al.*¹⁷ performed DFT calculations on two types of models of MoS₂/Au: (i) highly strained 1:1 epitaxial structures, where all S atoms are superimposed to top, or hollow Au sites and (ii) a simplified mismatched model aiming at reproducing the main features of the experimental moiré pattern, while still adopting a smaller supercell. The resulting interfacial distance was 2.51, 3.03, and 3.20 Å for the epitaxial top, hcp, and fcc structures, respectively, with a similar qualitative trend but remarkable quantitative differences, compared to the results reported in this paper. For their mismatched model, an average distance of 3.29 Å was reported.¹⁷ The much shorter average interfacial distance reported in our case (2.63 Å) is because of two factors, namely, the absence of major strain in our model and, most importantly, the inclusion of long-range dispersion forces in the potential (they were neglected in ref 17), which obviously brings the film closer to the support.

In our model, the interplanar distance between the Mo atoms and the S atoms is slightly contracted in the Au-supported film (1.56 Å) compared to the free-standing one (1.57 Å); this could be induced by the moderate tensile strain released on the film.

The MoS₂ ML adheres to Au(111) with an interaction energy of -60.52 meV/Å², largely because of dispersion forces. As suggested by the nonuniform interfacial distance (*vide supra*), this value is an average accounting for the presence of more strongly bound regions and weakly interacting regions across the moiré pattern. We also notice that the charge transfer from the substrate to the film (-15.6 millielectrons per MoS₂ formula unit) is very small, as also previously reported.¹⁴ This is different from the behavior of MoS₂ MLs in interaction to more reactive metal surfaces, which also confirms the van der Waals nature of the Au–MoS₂ interaction.⁴⁴ The interface dipole moment is almost negligible (-0.03 lel × Å). Nevertheless, a remarkable decrease of the work function with respect to the free Au surface is reported (-0.61 eV); in the absence of any sizable charge

transfer, this can most likely be attributed to compressive electrostatic effects.^{16,45}

The density of states (DOS) projected on S, Mo, and Au species is reported in Figure 3a. The Au Fermi level is pinned

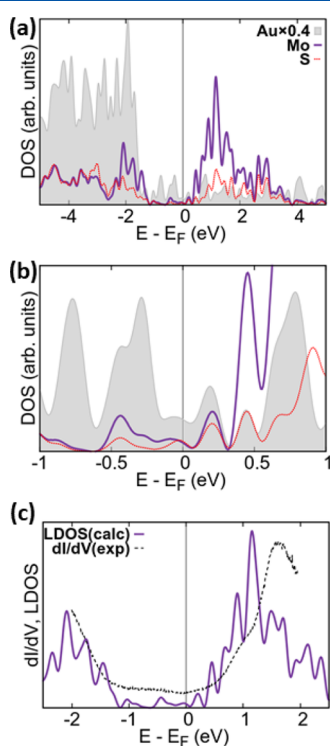


Figure 3. (a) DOS projected on Au, Mo, and S atoms (the contribution of Au atoms is rescaled by 0.4 for the sake of clarity). (b) Details of the DOS in the ± 1 eV region with respect to the Fermi level. (c) Comparison between the STS spectrum and local density of states (LDOS, projected on S and Mo orbitals).

well above the middle of the MoS₂ gap, as in an n-type contact, in agreement with previous reports.^{14,16,46} Both valence and conduction bands of MoS₂ display a predominant Mo (4d) character with a non-negligible S (3p) contribution. As evident from the detailed view of the states included within ± 1 eV from the Fermi level (Figure 3b), the film/support interaction is revealed by the presence of MoS₂ gap states [with a remarkable S (3p) component] because of the mixing with the Au surface orbitals. However, as also previously reported by Gong *et al.*,¹⁶ no covalent bond between Au and S atoms is established, as also revealed by XPS spectroscopy of MoS₂ growth on Au under various conditions.⁴⁷ A tentative comparison between the scanning tunneling spectroscopy (STS) and the local density of states projected on the Mo and S orbitals (LDOS) is shown in Figure 3c. As one can see, the main discrepancy between

experiment and calculations concerns the onset of the conduction band (that we approximately evaluated by looking at the maxima along the LDOS and STS curves), whose energy is underestimated by approximately 0.5 eV with our PBE + D approach; this reflects the underestimation of the calculated MoS₂ band gap, as discussed in the previous section. The onset of the valence band with respect to the Au Fermi level, on the contrary, is very well reproduced.

As discussed in detail in the literature,¹⁷ the Au–S local registry has an important effect on the electronic structure. In the present work, a large supercell accounting for the nonepitaxial nature of the MoS₂/Au interface is adopted, where regions displaying all possible Au–S registries coexist, as discussed above (see Figure 2c). The Tersoff–Hamann simulations at ± 0.5 eV (Figure 4a,b) fully account for the dependence of the substrate/film orbitals' mixing on the local registry: indeed, the S atoms lying in the top position display a more pronounced contrast in the simulated image because of their larger contribution to the partial charge density distribution. This feature reproduces the contrast of the experimental STM images, where the alternation of brighter and darker zones in the moiré pattern is clearly revealed (Figure 4c).^{21,22} The origin of this contrast, given the substantially planar nature of the MoS₂ film, is thus mainly to be attributed to electronic factors, as also supported by the fact that no dI/dV oscillations are reported between darker and brighter regions of the moiré pattern. As discussed in ref 17, the band edges of MoS₂ are remarkably perturbed in the presence of a stronger Au–S contact (such as in the top-stacking region), which supports the results hereby presented. Examining the lattice positions corresponding to the bright spots in the images, one can say that, regardless the sign of the bias potential, the dominating contribution to the images is because of S atoms. This is not surprising, given the non-negligible contribution of the S orbitals to the states lying close to the Fermi level (see the DOS plot reported in Figure 3b) and the apical position of the S atoms in the structure. It is important to state that the Tersoff–Hamann is a rather crude approximation, where an electron transport measurement such as the outcome of an STM scan is compared to a charge density map. A good match between the experiment and simulation, however, provides useful hints for the identification of the most common point defects in MoS₂/Au, as discussed in the next section.

3.2. Nature and Stability of Point Defects in MoS₂/Au.

The present study includes the analysis of several point defects. We first considered the removal of a single S atom, $V(S)$, or a single Mo atom, $V(Mo)$. Then, we moved to defect clusters such as the double sulfur vacancy, $V(S_2)$, or defects arising from the removal of a MoS₂, $V(MoS_2)$, or MoS₃, $V(MoS_3)$, units. In the case of $V(S_2)$, we also studied the nucleation effect, that is, the stability of the second S vacancy as a function of its distance from

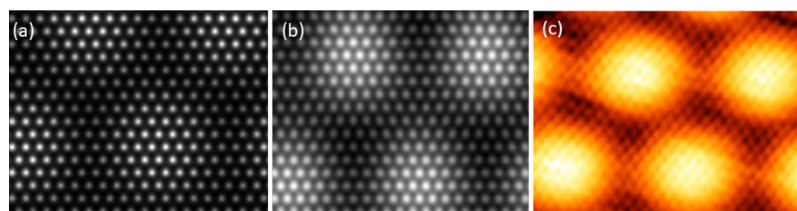


Figure 4. Tersoff–Hamann images at (a) -0.5 and (b) $+0.5$ eV compared to a high-resolution STM image of the moiré pattern (c), acquired at $+0.5$ V and 0.5 nA.

the first one. The choice to focus on these defects relies on former reports discussing their stability in the free-standing MoS₂ ML.^{24,25} Recently, the presence of point defects related to oxygen impurities incorporation has been proven for MoSe₂ films.⁴⁸ However, we rule out this option based on the scarce similarity of O-related defects with the D1 and D2 fingerprints in the STM images. Moving from the free-standing ML to the Au-supported film, the complexity of the system increases under two aspects: (i) the film/substrate interactions, which may affect the stability of the defects and (ii) the site heterogeneity, depending on the defect's location (outer or interfacial S layer) or on the local registry with respect to the Au surface.

The thermodynamic stability of the defective Mo_(1-x)S_(2-y)/Au structures has been checked with respect to their components. As references, we considered the pristine MoS₂/Au and elementary S and Mo in their most stable form, namely, the S₈ crystal and bulk Mo. The formation energy of the defect is then evaluated within the range of the S chemical potential, where MoS₂ is stable with respect to pure S (S-rich limit, $\mu_S = 0$) and bulk Mo (Mo-rich limit, $\mu_S = -1.25$ eV), Figure 5. The

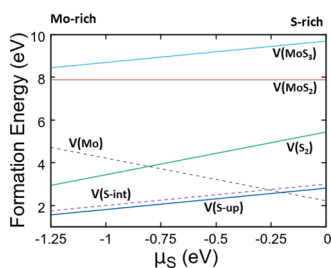


Figure 5. Formation energy of point defects as a function of the S chemical potential.

single sulfur vacancy formed on the upper layer, V(S-up), is the most stable defect over a wide range of μ_S , with a formation energy that varies from 1.55 eV (Mo-rich limit) to 2.81 eV (S-rich limit). A small effect because of the local registry of the defect site with respect to the metal substrate is observed: namely, V(S-up) is slightly more stable on a top site compared to hcp and fcc by 0.20 and 0.23 eV, respectively. For the sake of clarity, only the most stable case (*i.e.*, top) is shown in Figure 5. The single sulfur vacancy located at the film/support interface, V(S-int), has a formation energy slightly larger than V(S-up), spanning from 1.74 eV (Mo-rich limit) to 3.00 eV (S-rich limit). As in the case of V(S-up), the local registry plays a small role, and the hcp site is more stable than fcc and top by 0.13 and 0.17 eV, respectively (only the most favorable case is shown in Figure 5).

As shown in Figure 5, a stability crossover takes place close to the S-rich limit, where the Mo vacancy, V(Mo), becomes the most stable defect; in fact, V(Mo)'s formation energy drops from 4.73 eV (Mo-rich limit) to 2.22 eV (S-rich limit). It is worth reporting that the site's dependency of V(Mo)'s formation energy is more pronounced compared to sulfur vacancies, and V(Mo) is more stable on a hcp site compared to top and fcc sites by 0.36 and 0.39 eV, respectively. As for V(S), Figure 5 reports only the most favorable case.

The formation energies of larger defects, involving the removal of two or more atoms, are definitive less favorable. In the case of the disulfur vacancy, V(S₂), the formation energy spans from 2.93 eV (Mo-rich limit) to 5.44 eV (S-rich limit). Notably, this is only 7% less compared to the formation of two V(S) defects at infinite reciprocal distance, indicating a very

small tendency of vacancies toward dimerization, in analogy to what reported by DFT calculations on free-standing MoS₂ MLs²⁴ and at variance to what observed for other 2D materials such as graphene.⁴⁹ On Au-supported graphene/MoS₂, linear clusters of chalcogenide vacancies were observed.⁵⁰ Their presence was rationalized as an effect of the thermal annealing during the growth.

The removal of MoS₂ and MoS₃ units is highly unfavorable, displaying a formation energy at the Mo-rich limit as large as 7.90 and 8.43 eV. At the S-rich limit, the formation energy of V(MoS₃) further increases to 9.69 eV. Merging two V(S) and one V(Mo) to form V(MoS₂) is almost isoenergetic with respect to the separated point defects. The formation of V(MoS₃), on the contrary, shows a remarkable energy gain (0.96 eV) with respect to the cost to create three V(S) and one V(Mo). Large defects such as V(MoS₂) and V(MoS₃), however, result rather unstable compared to V(S) and V(Mo), regardless the chemical potential. In fact, large defects such as V(MoS₃) and even V(MoS₆) have been observed by transmission electron microscopy on MoS₂ ML supported on silica.²⁴ However, the electron beam involved in those measurements may cause some sputtering of S atoms, thus interfering with the defects' nature.⁵¹

It is not trivial to infer what are the actual experimental thermodynamic conditions of growth for MoS₂ deposited on gold. In general, PLD is assumed to mostly preserve the stoichiometry of the MoS₂ target. The subsequent annealing under UHV, however, may cause a loss of S atoms, thus leading to a sub-stoichiometric Mo/S ratio.⁵² It is thus reasonable to assume that the Mo-rich region in Figure 5 resembles more closely to the actual experimental growth conditions.

In summary, based on arguments of thermodynamic stability, one can state that single vacancies are more easily formed compared to clusters of vacancies in the case of in MoS₂/Au. We will now look at the defect's appearance in the Tersoff–Hamann images prior to try an assignment of the more common defect of fingerprints detected by STM measurements (a circle, D1, and a triangle, D2, Figure 1b). All images are realized at a bias potential of +0.5 eV (in analogy to the experiments), as shown in Figure 6.

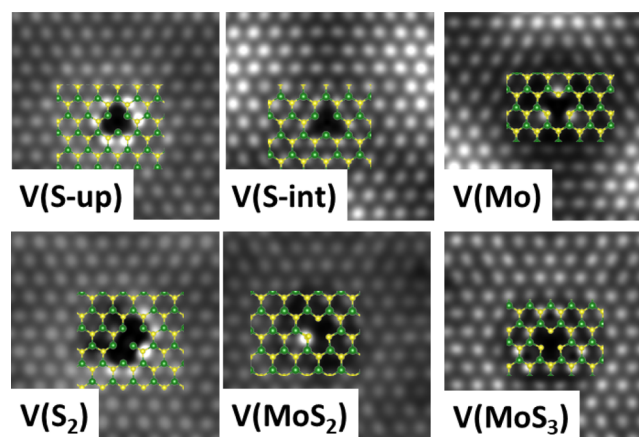


Figure 6. Tersoff–Hamann images of point defects in MoS₂/Au.

A common feature to all defects is the appearance of a darker area, where atoms are removed in the MoS₂/Au moiré pattern, often surrounded by very bright spots, attributed to empty orbitals localized on atoms close to the defect and lying within the Fermi level and the bias potential. The contrast with the surroundings is also influenced by the registry because point

defects can be located in brighter (top) or darker (fcc, hcp) regions (only images referring to the minimum energy case are reported in Figure 6 for simplicity). The main criterion to differentiate the images of the defects is the shape of the darker region. In the case of V(S), interestingly, the image changes remarkably depending if the vacancy is located on the upper S layer, V(S-up), or at the interface, V(S-int): in the former case, a dark spot surrounded by six bright spots is reported, while in the latter, the vacancy leaves a triangular fingerprint with very well-defined borders.

V(Mo) has a more complex image, appearing as a darker roughly hexagonal zone enclosing three single, very bright spots (corresponding to the top S atoms directly bound to the removed Mo). This image, however, is remarkably different from the D2 defect as detected by STM (see Figure 1b), where the triangular shape displays bright sides, while in the V(Mo)'s simulated image, only the three corners display high contrast.

The V(S₂) defect has an ellipsoidal shape similar to the junction of two V_S images. If also a Mo atom is removed, forming V(MoS₂), the main new feature is a bright single spot at the boundary of the ellipse. V(MoS₃), finally, displays a large and very well-defined truncated triangle feature.

A combined analysis of the simulated images and the data on the thermodynamic stability of defects suggests an assignment for the main defective features evidenced by STM measurements, D1 and D2, as V(S-up) and V(S-int), respectively. Indeed, the polygonal and triangle features in the Tersoff–Hamann images resemble those evidenced experimentally, and V(S) species is more stable than any other defect over a wide range of S chemical potential. Also, the scarce dependence of V(S) stability on the local registry with the metal substrate fits with the ubiquitous nature of D1 and D2 over the different domains of the moiré pattern.²² It must be pointed out, however, that a 1:1 comparison between the STM images of D1 and D2 features and the Tersoff–Hamann images of the defective structures reported in Figure 6 is perhaps an oversimplification. Moreover, some details do not fully fit (for instance, the sides of the triangular D2 defects appear brighter than the surrounding in the STM images, while they display the same contrast as the surrounding in the calculated images). These discrepancies can be attributed to the intrinsic limits of the Tersoff–Hamann approach. As discussed in Section 3.1, moreover, the alignment of the defect's states with respect to the Au Fermi level may show some small offset with respect to the experiment. However, one can positively say that (i) the appearance of triangular shapes in the STM images is not necessarily related to the presence of vacancies' clusters and (ii) S-vacancies display different shapes depending on their location. This latter aspect needs to be better explained. In a previous report on the intrinsic nature of point defects in MoS₂, the authors resorted to calculations on the free-standing MoS₂ ML to infer the shape of the defect's state related to the formation of an S vacancy.²³ Interestingly, they found that, upon removal of an S atom, a deep gap state with triangular symmetry and a shallow one with spherical symmetry are created. One could thus explain the different shapes of V(S-up) and V(S-int) images in terms of different mixing of the defect's state with the metal substrate and variation of their related energies with respect to the Au Fermi level for sites lying at the interface or on the upper surface. This hypothesis is confirmed by the DOS plot reported in Figure 7. The plot shows the DOS projected on the three Mo atoms directly connected to the removed S atom for V(S-up) and V(S-int). The difference between these two cases is evident: for V(S-up), one obtains a

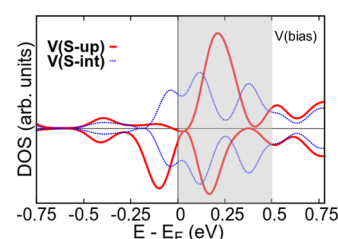


Figure 7. DOS projected on the Mo atoms close to the vacancy for V(S-up) and V(S-int). The energy range, V(bias), enclosed in the Tersoff–Hamann images from Figure 6 is highlighted in gray.

spin-polarized solution with an occupied state very close to the Fermi level and a degenerate empty state well within the energy range enclosed in the bias potential adopted to generate the Tersoff–Hamann images (+0.5 eV). For V(S-int), the defect states are blurred and shifted to higher energy as a consequence of the mixing with the Au surface's orbitals, which justifies the difference in shape observed experimentally and confirmed by the hereby reported simulations.

It is finally interesting to notice how the tendency toward defects' clustering is different for MoS₂/Au compared to free-standing MoS₂ [where V(MoS₃) was found to be more stable than the separated vacancies].^{24,25} All these arguments highlight the necessity to perform large-scale simulation over a realistic model of the MoS₂/Au interface in order to reach a detailed picture of the structure as well as a solid assignment of its point defects.

4. CONCLUSIONS

This paper investigates the Au–MoS₂ interface and the nature of the point defects in the supported film by means of DFT calculations and STM measurements. To the best of our knowledge, a realistic model of the wide 10 × 10/11 × 11 MoS₂/Au superlattice has been simulated here for the first time. The noncommensurate interface formed upon growth of MoS₂ ML on Au(111) leads to a moiré pattern characterized by the coexistence of different film/substrate registries. As revealed by the calculations, the interfacial distance depends remarkably on the registry, and where a top S–Au coincidence is present, the Au atoms are uplifted as an effect of the bond to the film. This is a clear sign that the interaction is locally stronger, where a favorable registry is established. The interplay between the film and substrate and its dependence on the registry is well visible in the STM images, displaying a hexagonal arrangement of brighter and darker zones. This feature is substantially reproduced by Tersoff–Hamann images, showing how the domains, where the match between apical Au atoms and bottom S atoms, better appear as brighter regions in the image.

MoS₂ MLs supported on gold are quite abundant in vacancies, a feature with relevant implication for their conductivity and thus their application in microelectronics, for instance. Experimentally, two very abundant fingerprints of point defects are detected in STM images, displaying circular and triangular shapes, respectively. An extensive analysis of the calculated formation energies of several kind of single vacancies and vacancies' clusters, considering also the effect of the local registry with respect to the Au support, leads to following remarks:

- The most stable defects over a wide range of S chemical potential are single sulfur vacancies, V(S), either located on the apical layer of S atoms or at the interface with Au.

Their stability is not remarkably affected by the local registry with Au.

- The single Mo vacancy is more stable than the S vacancy only under strong sulfur-rich conditions, which most likely does not fit to the real growth conditions. $V(\text{Mo})$ exhibits a stronger dependence on the registry compared to $V(\text{S})$.
- The tendency toward vacancies clustering, forming $V(\text{S}_2)$, $V(\text{MoS}_2)$, or $V(\text{MoS}_3)$, is less pronounced for MoS_2/Au compared to free-standing MoS_2 or SiO_2 -supported MoS_2 .

The analysis of the Tersoff–Hamann images of these defects shows that interfacial or apical sulfur vacancies display triangular and circular shapes, with some similarities to the experimentally detected D1 and D2 species. One may thus conclude that the most common defect on MoS_2/Au is indeed constituted by single $V(\text{S})$, rather than defects' clusters. The difference in shape between the Tersoff–Hamann images of apical and interfacial $V(\text{S})$ can be rationalized in terms of shifts of the related states as an effect of the mixing with Au states.

AUTHOR INFORMATION

Corresponding Author

Sergio Tosoni – Dipartimento di Scienza dei Materiali, Università di Milano-Bicocca, 21025 Milano, Italy; orcid.org/0000-0001-5700-4086; Phone: +39-02-64485214; Email: sergio.tosoni@unimib.it

Authors

Francesco Tumino – Department of Energy, Politecnico di Milano, 20133 Milano, Italy; orcid.org/0000-0002-4846-2701

Carlo Spartaco Casari – Department of Energy, Politecnico di Milano, 20133 Milano, Italy; orcid.org/0000-0001-9144-6822

Andrea Li Bassi – Department of Energy, Politecnico di Milano, 20133 Milano, Italy

Complete contact information is available at: <https://pubs.acs.org/10.1021/acs.jpcc.0c01477>

Notes

The authors declare no competing financial interest.

ACKNOWLEDGMENTS

S.T. acknowledges the financial support from the Italian Ministry for University and Research (MIUR) through the program Dipartimenti di Eccellenza-2017 “Materials For Energy” and CINECA supercomputing centre for the access to high-performing computing resources under the ISCRAB initiative.

REFERENCES

- (1) Wang, Q. H.; Kalantar-Zadeh, K.; Kis, A.; Coleman, J. N.; Strano, M. S. Electronics and Optoelectronics of Two-Dimensional Transition Metal Dichalcogenides. *Nat. Nanotechnol.* **2012**, *7*, 699–712.
- (2) Splendiani, A.; Sun, L.; Zhang, Y.; Li, T.; Kim, J.; Chim, C.-Y.; Galli, G.; Wang, F. Emerging Photoluminescence in Monolayer MoS_2 . *Nano Lett.* **2010**, *10*, 1271–1275.
- (3) Mak, K. F.; Lee, C.; Hone, J.; Shan, J.; Heinz, T. F. Atomically Thin MoS_2 : A New Direct-Gap Semiconductor. *Phys. Rev. Lett.* **2010**, *105*, 136805.
- (4) Radisavljevic, B.; Radenovic, A.; Brivio, J.; Giacometti, V.; Kis, A. Single-Layer MoS_2 Transistors. *Nat. Nanotechnol.* **2011**, *6*, 147–150.

- (5) Chianelli, R. R.; Siadati, M. H.; De la Rosa, M. P.; Berhault, G.; Wilcoxon, J. P.; Bearden, R.; Abrams, B. L. Catalytic Properties of Single Layers of Transition Metal Sulfide Catalytic Materials. *Catal. Rev.* **2006**, *48*, 1–41.

- (6) Zou, X.; Zhang, Y. Noble Metal-Free Hydrogen Evolution Catalysts for Water Splitting. *Chem. Soc. Rev.* **2015**, *44*, S148–S180.

- (7) Tan, Y.; Liu, P.; Chen, L.; Cong, W.; Ito, Y.; Han, J.; Guo, X.; Tang, Z.; Fujita, T.; Hirata, A.; et al. Monolayer MoS_2 Films Supported by 3D Nanoporous Metals for High-Efficiency Electrocatalytic Hydrogen Production. *Adv. Mater.* **2014**, *26*, 8023–8028.

- (8) Yazyev, O. V.; Kis, A. MoS_2 and Semiconductors in the Flatland. *Mater. Today* **2015**, *18*, 20–30.

- (9) Noh, J.-Y.; Kim, H.; Kim, Y.-S. Stability and Electronic Structures of Native Defects in Single-Layer MoS_2 . *Phys. Rev. B: Condens. Matter Phys.* **2014**, *89*, 205417.

- (10) Hong, J.; Hu, Z.; Probert, M.; Li, K.; Lv, D.; Yang, X.; Gu, L.; Mao, N.; Feng, Q.; Xie, L.; et al. Exploring Atomic Defects in Molybdenum Disulfide Monolayers. *Nat. Commun.* **2015**, *6*, 6293.

- (11) Su, J.; Li, N.; Zhang, Y.; Feng, L.; Liu, Z. Role of Vacancies in Tuning the Electronic Properties of Au- MoS_2 Contact. *AIP Adv.* **2015**, *5*, 077182.

- (12) Freund, H.-J.; Pacchioni, G. Oxide Ultra-Thin Films on Metals: New Materials for the Design of Supported Metal Catalysts. *Chem. Soc. Rev.* **2008**, *37*, 2224–2242.

- (13) Giordano, L.; Pacchioni, G. Oxide Films at the Nanoscale: New Structures, New Functions, and New Materials. *Acc. Chem. Res.* **2011**, *44*, 1244–1252.

- (14) Popov, I.; Seifert, G.; Tománek, D. Designing Electrical Contacts to MoS_2 Monolayers: A Computational Study. *Phys. Rev. Lett.* **2012**, *108*, 156802.

- (15) Kang, J.; Liu, W.; Sarkar, D.; Jena, D.; Banerjee, K. Computational Study of Metal Contacts to Monolayer Transition-Metal Dichalcogenide Semiconductors. *Phys. Rev. X* **2014**, *4*, 031005.

- (16) Gong, C.; Colombo, L.; Wallace, R. M.; Cho, K. The Unusual Mechanism of Partial Fermi Level Pinning at Metal- MoS_2 Interfaces. *Nano Lett.* **2014**, *14*, 1714–1720.

- (17) Bruix, A.; Miwa, J. A.; Hauptmann, N.; Wegner, D.; Ulstrup, S.; Grønberg, S. S.; Sanders, C. E.; Dendzik, M.; Grubišić Čabo, A.; Bianchi, M.; et al. Single-Layer MoS_2 on Au(111): Band Gap Renormalization and Substrate Interaction. *Phys. Rev. B* **2016**, *93*, 165422.

- (18) Van Hove, M. A.; Koestner, R. J.; Stair, P. C.; Bibérian, J. P.; Kesmodel, L. L.; Bartoš, I.; Somorjai, G. A. The Surface Reconstructions of the (100) Crystal Faces of Iridium, Platinum and Gold. I. Experimental Observations and Possible Structural Models. *Surf. Sci.* **1981**, *103*, 189–217.

- (19) Harten, U.; Lahee, A. M.; Toennies, J. P.; Wöll, C. Observation of a Soliton Reconstruction of Au(111) by High-Resolution Helium-Atom Diffraction. *Phys. Rev. Lett.* **1985**, *54*, 2619–2622.

- (20) Grønberg, S. S.; Ulstrup, S.; Bianchi, M.; Dendzik, M.; Sanders, C. E.; Lauritsen, J. V.; Hofmann, P.; Miwa, J. A. Synthesis of Epitaxial Single-Layer MoS_2 on Au(111). *Langmuir* **2015**, *31*, 9700–9706.

- (21) Krane, N.; Lotze, C.; Franke, K. J. Moiré Structure of MoS_2 on Au(111): Local Structural and Electronic Properties. *Surf. Sci.* **2018**, *678*, 136–142.

- (22) Tumino, F.; Casari, C. S.; Passoni, M.; Russo, V.; Li Bassi, A. Pulsed Laser Deposition of Single-Layer MoS_2 on Au(111): From Nanosized Crystals to Large-Area Films. *Nanoscale Adv.* **2019**, *1*, 643–655.

- (23) Vancsó, P.; Magda, G. Z.; Pető, J.; Noh, J.-Y.; Kim, Y.-S.; Hwang, C.; Biró, L. P.; Tapasztó, L. The Intrinsic Defect Structure of Exfoliated MoS_2 Single Layers Revealed by Scanning Tunneling Microscopy. *Sci. Rep.* **2016**, *6*, 29726.

- (24) Zhou, W.; Zou, X.; Najmaei, S.; Liu, Z.; Shi, Y.; Kong, J.; Lou, J.; Ajayan, P. M.; Yakobson, B. I.; Idrobo, J.-C. Intrinsic Structural Defects in Monolayer Molybdenum Disulfide. *Nano Lett.* **2013**, *13*, 2615–2622.

- (25) Komsa, H.-P.; Krasheninnikov, A. V. Native Defects in Bulk and Monolayer MoS_2 from First Principles. *Phys. Rev. B* **2015**, *91*, 125304.

- (26) Bruix, A.; Lauritsen, J. V.; Hammer, B. Effects of Particle Size and Edge Structure on the Electronic Structure, Spectroscopic Features, and Chemical Properties of Au(111)-Supported MoS₂ Nanoparticles. *Faraday Discuss.* **2016**, *188*, 323–343.
- (27) Robinson, B. J.; Giusca, C. E.; Gonzalez, Y. T.; Kay, N. D.; Kazakova, O.; Kolosov, O. V. Structural, Optical and Electrostatic Properties of Single and Few-Layers MoS₂: Effect of Substrate. *2D Mater.* **2015**, *2*, 015005.
- (28) Kresse, G.; Hafner, J. Ab Initio Molecular Dynamics for Liquid Metals. *Phys. Rev. B: Condens. Matter Mater. Phys.* **1993**, *47*, 558–561.
- (29) Kresse, G.; Furthmüller, J. Efficiency of Ab-Initio Total Energy Calculations for Metals and Semiconductors Using a Plane-Wave Basis Set. *Comput. Mater. Sci.* **1996**, *6*, 15–50.
- (30) Blöchl, P. E. Projector Augmented-Wave Method. *Phys. Rev. B: Condens. Matter Mater. Phys.* **1994**, *50*, 17953–17979.
- (31) Kresse, G.; Joubert, D. From Ultrasoft Pseudopotentials to the Projector Augmented-Wave Method. *Phys. Rev. B: Condens. Matter Mater. Phys.* **1999**, *59*, 1758–1775.
- (32) Perdew, J. P.; Burke, K.; Ernzerhof, M. Generalized Gradient Approximation Made Simple. *Phys. Rev. Lett.* **1996**, *77*, 3865–3868.
- (33) Grimme, S.; Antony, J.; Ehrlich, S.; Krieg, H. A Consistent and Accurate Ab Initio Parametrization of Density Functional Dispersion Correction (DFT-D) for the 94 Elements H-Pu. *J. Chem. Phys.* **2010**, *132*, 154104.
- (34) Neugebauer, J.; Scheffler, M. Adsorbate-Substrate and Adsorbate-Adsorbate Interactions of Na and K Adlayers on Al(111). *Phys. Rev. B: Condens. Matter Mater. Phys.* **1992**, *46*, 16067–16080.
- (35) Massalski, T. B.; Okamoto, H. *Binary Alloy Phase Diagrams*; ASM International: Materials Park, Ohio, USA, 1990.
- (36) Schönfeld, B.; Huang, J. J.; Moss, S. C. Anisotropic Mean-square Displacements (MSD) in Single-crystals of 2H- and 3R-MoS₂. *Acta Crystallogr., Sect. B: Struct. Sci.* **1983**, *39*, 404–407.
- (37) Cheiwchanchamnangij, T.; Lambrecht, W. R. L. Quasiparticle Band Structure Calculation of Monolayer, Bilayer, and Bulk MoS₂. *Phys. Rev. B: Condens. Matter Mater. Phys.* **2012**, *85*, 205302.
- (38) Ramasubramaniam, A. Large Excitonic Effects in Monolayers of Molybdenum and Tungsten Dichalcogenides. *Phys. Rev. B: Condens. Matter Mater. Phys.* **2012**, *86*, 115409.
- (39) Liang, Y.; Huang, S.; Soklaski, R.; Yang, L. Quasiparticle Band-Edge Energy and Band Offsets of Monolayer of Molybdenum and Tungsten Chalcogenides. *Appl. Phys. Lett.* **2013**, *103*, 042106.
- (40) Beal, A. R.; Hughes, H. P. Kramers-Kronig Analysis of the Reflectivity Spectra of 2H-MoS₂, 2H-MoSe₂ and 2H-MoTe₂. *J. Phys. C: Solid State Phys.* **1979**, *12*, 881–890.
- (41) Sørensen, S. G.; Füchtbauer, H. G.; Tuxen, A. K.; Walton, A. S.; Lauritsen, J. V. Structure and Electronic Properties of In Situ Synthesized Single-Layer MoS₂ on a Gold Surface. *ACS Nano* **2014**, *8*, 6788–6796.
- (42) Kokkin, D. L.; Zhang, R.; Steimle, T. C.; Wyse, I. A.; Pearlman, B. W.; Varberg, T. D. Au-S Bonding Revealed from the Characterization of Diatomic Gold Sulfide, AuS. *J. Phys. Chem. A* **2015**, *119*, 11659–11667.
- (43) Bürgi, T. Properties of the Gold-Sulphur Interface: From Self-Assembled Monolayers to Clusters. *Nanoscale* **2015**, *7*, 15553–15567.
- (44) Chen, W.; Santos, E. J. G.; Zhu, W.; Kaxiras, E.; Zhang, Z. Tuning the Electronic and Chemical Properties of Monolayer MoS₂ Adsorbed on Transition Metal Substrates. *Nano Lett.* **2013**, *13*, 509–514.
- (45) Prada, S.; Martinez, U.; Pacchioni, G. Work Function Changes Induced by Deposition of Ultrathin Dielectric Films on Metals: A Theoretical Analysis. *Phys. Rev. B: Condens. Matter Mater. Phys.* **2008**, *78*, 235423.
- (46) Farmanbar, M.; Brocks, G. Controlling the Schottky Barrier at MoS₂/Metal Contacts by Inserting a BN Monolayer. *Phys. Rev. B* **2015**, *91*, 161304.
- (47) Smyth, C. M.; Addou, R.; McDonnell, S.; Hinkle, C. L.; Wallace, R. M. Contact Metal-MoS₂ Interfacial Reactions and Potential Implications on MoS₂-Based Device Performance. *J. Phys. Chem. C* **2016**, *120*, 14719–14729.
- (48) Barja, S.; Refaely-Abramson, S.; Schuler, B.; Qiu, D. Y.; Pulkin, A.; Wickenburg, S.; Ryu, H.; Ugeda, M. M.; Kastl, C.; Chen, C.; et al. Identifying Substitutional Oxygen as a Prolific Point Defect in Monolayer Transition Metal Dichalcogenides. *Nat. Commun.* **2019**, *10*, 1–8.
- (49) Lee, G.-D.; Wang, C. Z.; Yoon, E.; Hwang, N.-M.; Kim, D.-Y.; Ho, K. M. Diffusion, Coalescence, and Reconstruction of Vacancy Defects in Graphene Layers. *Phys. Rev. Lett.* **2005**, *95*, 205501.
- (50) Liu, M.; Shi, J.; Li, Y.; Zhou, X.; Ma, D.; Qi, Y.; Zhang, Y.; Liu, Z. Semiconductors: Temperature-Triggered Sulfur Vacancy Evolution in Monolayer MoS₂/Graphene Heterostructures. *Small* **2017**, *13*, 1602967.
- (51) Komsa, H.-P.; Kotakoski, J.; Kurasch, S.; Lehtinen, O.; Kaiser, U.; Krasheninnikov, A. V. Two-Dimensional Transition Metal Dichalcogenides under Electron Irradiation: Defect Production and Doping. *Phys. Rev. Lett.* **2012**, *109*, 035503.
- (52) Donarelli, M.; Bisti, F.; Perrozzi, F.; Ottaviano, L. Tunable Sulfur Desorption in Exfoliated MoS by Means of Thermal Annealing in Ultra-High Vacuum. *Chem. Phys. Lett.* **2013**, *588*, 198–202.